Geophysical Journal International

Geophys. J. Int. (2023) **232,** 1259–1275
Advance Access publication 2022 October 06
GJI Seismology

https://doi.org/10.1093/gji/ggac389

An analysis of core–mantle boundary related seismic waves using full-waveform modelling and adjoint methods

Maria Koroni [1], Anselme Borgeaud,[2] Andreas Fichtner [3] and Frédéric Deschamps[2]

[1] *Swiss Seismological Service, ETH Zürich, Sonneggstrasse* 5, 8092 *Zürich, Switzerland. E-mail: maria.koroni@sed.ethz.ch*
[2] *Institute of Earth Sciences, Academia Sinica,* 128 *Academia Road, Sector* 2, *Nangang, Taipei* 11529, *Taiwan*
[3] *Department of Earth Sciences, Institute of Geophysics, ETH Zürich, Sonneggstrasse* 5, 8092 *Zürich, Switzerland*

Accepted 2022 October 3. Received 2022 September 12; in original form 2021 August 2

SUMMARY

The core–mantle boundary (CMB) is the most abrupt internal discontinuity in the Earth, marking the solid–fluid boundary between mantle and outer core that strongly affects the dynamics of the Earth's interior. However, good agreement between models of CMB topographic variations is still lacking. This is probably due to difficulties relating to observations on seismograms and to the lack of good models of lowermost mantle velocity structure. Using spectral-element synthetic seismograms and adjoint methods, we perform traveltime analyses of seismic waves interacting with the CMB. We focus on reflected and refracted *P* and *S* waves. We select some of the most important and routinely used seismic phases: *ScS, SKS, SKKS, PcP, PKP, PKKP* and *PcS*, given their path through mantle and core and their interaction with the CMB. These seismic waves have been widely deployed by seismologists trying to image CMB topography and lowermost mantle structure. To analyse the reliability of measuring their traveltimes to infer CMB topography, we perform experiments in two ways. First, we compute synthetic seismograms with a dominant period of $T \approx 11$s, for computational efficiency, using existing models of CMB topography. We compare traveltime perturbations measured by cross-correlation on the synthetics to those predicted using ray theory. We find deviations from a perfect agreement between ray theoretical predictions of time shifts and those measured on synthetics with and without CMB topography. Second, we calculate Fréchet sensitivity kernels of traveltimes with respect to shear and compressional wave speeds. We also explicitly compute boundary sensitivities with respect to the CMB interface. We observe that the overall sensitivity of the traveltimes is mostly due to volumetric velocity structure and that imprints of CMB on traveltimes are less pronounced. Our study explains the observed difficulties relating to inferring CMB topography using traveltimes and provides a suite of finite frequency sensitivity kernels computed with the adjoint method. The kernels allow us to qualitatively explain the behaviour of measured traveltimes and understand the trade-off between velocity and CMB topography. They can also serve as reference of finite frequency effects on traveltimes of observed seismic phases. From our analyses we conclude that: i) traveltime anomalies measured on *S* waves are more in accord with ray theoretical predictions, ii) *PcP, PKP, ScS* and *SKS* phases have more pronounced sensitivity to the boundary and iii) separating the greater effects of velocity from those due to the boundary structure is difficult, as they intricately affect the traveltime. We propose that jointly inverting for CMB topography and lowermost mantle velocity structure using full-waveform synthetics and adjoint sensitivity kernels can progress our understanding of deep Earth structure and finite frequency effects on observed waveforms.

Key words: Body waves; Computational seismology; Wave propagation; Finite frequency kernels; Core–mantle boundary.

1 INTRODUCTION

The core–mantle boundary (CMB) is a major and sharp discontinuity inside the Earth, separating the mantle, which is composed of solid material mainly consisting of bridgmanite or post-perovskite and magnesiowüstite (Mattern *et al.* 2005), from the outer core, which is mainly consisting of liquid iron and nickel alloy. Along this interface major interactions between the lower mantle and the outer core occur (e.g. Stevenson 1981; Gurnis *et al.* 1998; Jeanloz & Williams 1998; Lay *et al.* 1998; Helffrich & Wood 2001). These interactions influence mantle and core processes, for example the geodynamo, and therefore the Earth's magnetic field. Key phenomena affecting the Earth's evolution and dynamics take place on each side of the CMB. Specifically, on the mantle side the CMB region is believed to be the source of mantle plumes which trigger intraplate volcanism at the Earth's surface, whilst on the core side magneto-hydrodynamic flow shapes magnetic field lines that are partially controlling the magnetic field along the CMB.

Developments of consistent models of the mantle structure and dynamics above the boundary can improve geodynamo modelling (e.g. Bloxham & Jackson 1992) and explain fundamental processes, such as the influence of the heat flux at the CMB, imposed by mantle dynamics, on the geodynamo (e.g. Amit *et al.* 2015). Lateral variations of the CMB radius, with its aspherical structure, may affect outer core flow processes implying that a better image of CMB topography is essential for analyses of gravitational and topographic coupling between mantle and core (e.g. Gubbins & Richards 1986; Calkins *et al.* 2012; Davies *et al.* 2014).

Thus, the CMB and its topography as well as the seismic structure of the D″ layer above it are perhaps the most interesting regions for interdisciplinary geophysical research. From a seismological perspective, however, it is difficult to resolve the velocity structure and topographic variations robustly because of their strong trade-offs Over the years, a great amount of seismological research has focused on inverting for lower-mantle boundary and CMB topography structure using *P*- and *S*-seismic phases (e.g. Creager & Jordan 1986; Morelli & Dziewonski 1987; Doornbos & Hilton 1989; Rodgers & Wahr 1993; Obayashi & Fukao 1997; Sze & van der Hilst 2003; Restivo & Helffrich 2006; Tanaka 2010; Wu *et al.* 2014; Mancinelli & Shearer 2016; Schlaphorst *et al.* 2016; Shen *et al.* 2016) as well as normal modes (e.g. Li *et al.* 1991; Ishii & Tromp 1999; Soldati *et al.* 2013).

However, existing differences among suggested CMB topography models even for spherical harmonic degrees higher than two (e.g. Becker & Boschi 2002; Koelemeijer 2021) indicate that there may be features of the lowermost mantle structure that need to be taken into account more systematically. Possible inaccuracies in interpreting observed data can also be a reason for these differences, as most studies are usually based on linearized ray theory.

Undoubtedly, an important factor that hinders a more accurate imaging of CMB topographic structure is the poorly understood complexity of the seismic structure in the bottom 300–400 km of the mantle. This includes the D″ discontinuity, which is not present everywhere and, therefore, has not been confirmed as a global feature in current Earth models. This discontinuity is consistent with the phase transition from bridgmanite to post-perovskite (e.g. Cobden *et al.* 2015; Hirose *et al.* 2017). This lowermost mantle layer is also characterized by evidence for ultralow velocity zones (ULVZs), which are thin pockets where compressional and shear wave velocities (V_P and V_S) drop by up to 10 per cent and 30 per cent, respectively (e.g. Yu & Garnero 2018), while some other studies suggested even larger drops in V_S of about 45 per cent (Thorne *et al.* 2013) and 24 per cent in V_P (Brown *et al.* 2015; Krier *et al.* 2021). Additional strong, small-scale anomalies due to cold oceanic slab material that has been subducted down to the CMB have been reported (e.g. Hung. *et al.* 2005; Whittaker *et al.* 2015; Borgeaud *et al.* 2017).

Studies have also shown the existence of large low shear wave velocity provinces (LLSVPs) defined as regions spanning a few thousands of kilometers, where shear velocity drops by a few percent and which are located beneath Africa and the Pacific ocean (e.g. Li & Romanowicz 1996; Ritsema *et al.* 2011; Lekic *et al.* 2012; Garnero *et al.* 2016; McNamara 2018). Because they may be closely related to mantle dynamics, LLSVPs may strongly influence CMB topography. Geodynamic modelling using numerical simulations showed that depending on their exact nature, either purely thermal or thermo-chemical, LLSVPs would trigger either uplifts or depressions along the CMB (Lassak *et al.* 2010; Deschamps *et al.* 2018).

Constraining the complex lowermost mantle velocity structure is essential in order to properly map topographic variations along the CMB. Ideally, one would like to resolve CMB topography structure, while simultaneously obtaining an updated velocity model for the 3-D lowermost mantle (e.g. Soldati *et al.* 2012; Colombi *et al.* 2014) instead of treating them independently. It has been shown by many researchers that CMB topography and mantle velocity variations exhibit strong trade-off, which makes the inference of CMB topography a hard task, when these two parameters are not synchronously inverted for (e.g. Garcia & Souriau 2000; Sze & van der Hilst 2003; Koelemeijer *et al.* 2012).

To date, many studies have been dedicated to the inference of lowermost mantle compressional and shear wave speed structure using several related body wave phases as well as differential traveltimes between these (e.g. Li & Romanowicz 1996; Garnero 2000; Tanaka 2002; Ritsema *et al.* 2011; Lekic *et al.* 2012; Garnero *et al.* 2016; Muir & Tkalčić 2020). A summary of the progress made during the last decades and relevant literature can be found in Gurnis *et al.* (1998), Garnero (2000) and Koelemeijer (2021).

Using a different approach, the studies by Colombi *et al.* (2012, 2014), based on axisymmetric spectral-element modelling (Nissen-Meyer *et al.* 2014), have implemented boundary and volume sensitivity kernels within a spectral-element code given spherically symmetric background models. They used this implementation to address the sensitivity of $P_{\rm diff}$, *PKP, PcP* and *ScS* and showed a suite of sensitivity kernels with respect to CMB structure (Colombi *et al.* 2012). Their research gave great insights into how to incorporate sensitivity of traveltimes of the seismic phases $P_{\rm diff}$, *PKP, PcP* and *ScS* for imaging the CMB in a joint inversion for boundary and lowermost mantle velocity structure (Colombi *et al.* 2014).

More specifically, they performed a broad-band waveform inversion and showed that for the source–receiver geometries corresponding to *PKP, PcP* and *ScS*, their inversion approach can be successfully used to invert for long-wavelength CMB topographic variations using cross-correlation traveltime measurements. On the other hand, they found that $P_{\rm diff}$ is not well-suited for inferring topography at CMB.

They have also showed that correcting for 3-D velocity structure in order to infer CMB topography leads to inaccurate inferences, due to disagreements between *P*- and *S*-velocity models. They suggested simultaneously inverting for 3-D mantle structure and CMB topography using finite frequency sensitivity kernels. They advocated that jointly inverting for 3-D structure and CMB topography is the only reliable way to properly account for the intricate trade-off of topography and mantle effects on traveltime data.

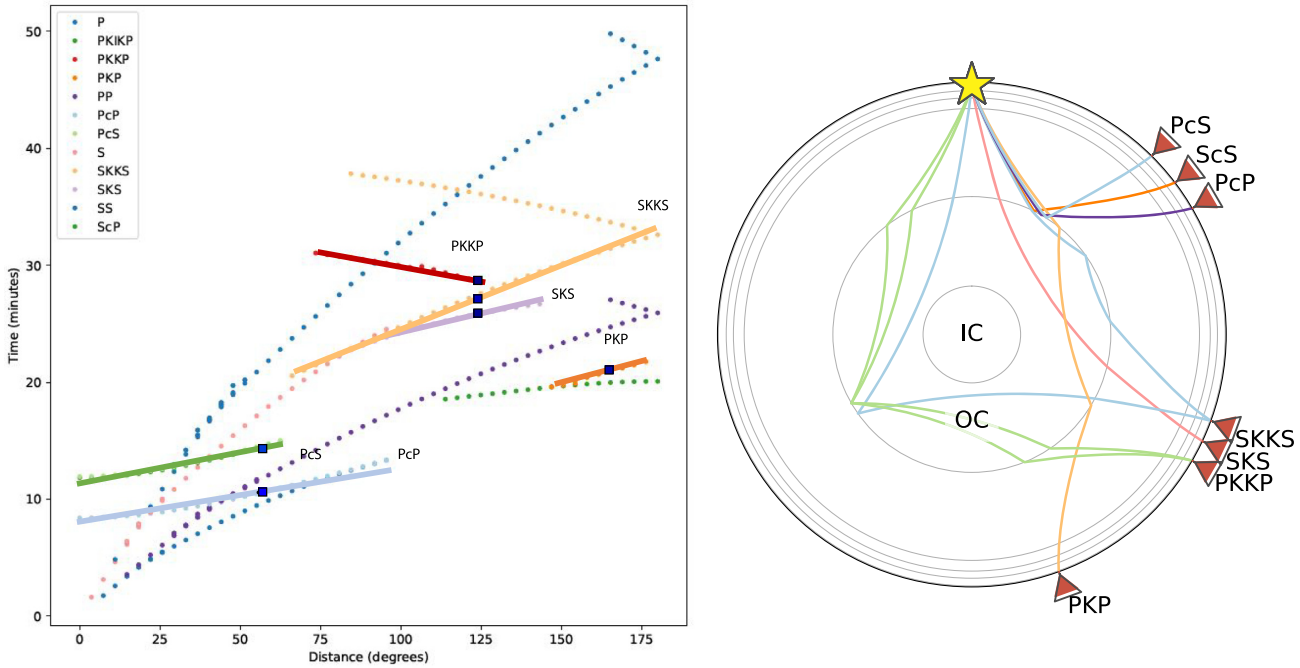

Figure 1. Left: traveltime curves according to model PREM and tauP (Crotwell *et al.* 1999). The phases we investigate in this work are drawn with solid lines. More primary phases are plotted in order to justify the chosen epicentral distances for the sensitivity analysis. The characteristic distances chosen for computing the sensitivity kernels are shown by blue circles on the solid lines for each phase. Right: Theoretical ray paths for the same model. Red triangles denote stations at the epicentral distances were we opt observing the phases for the sensitivity analysis. The colours in the two subfigures are not corresponding. IC denotes inner core, OC denotes outer core.

Our study is based on a similar approach; it, however, solely focuses on analysing the sensitivity of some of the most informative and widely used *P*- and *S*-body wave phases. Motivated by the findings of Colombi *et al.* (2012, 2014), although using a different numerical tool, we calculate full-waveform synthetics with spectral elements on a cubed sphere, as implemented in SPECFEM3D_GLOBE (Komatitsch & Tromp 1999, 2002a,b), where the global wave propagation effects can accurately be accounted for and consistently implemented into 3-D full-waveform inversion (FWI) schemes for CMB topography. The goal of our study is twofold. First, We investigate a suite of *P*- and *S*-wave phases and their traveltimes, which are observed in synthetic seismograms. These are computed with a resolvable dominant period of T≈11 seconds. We focus on the seismic phases *PcP, PKP, PKKP, PcS, ScS, SKS* and *SKKS*. These body wave phases are frequently used in seismological studies, which aim at mapping CMB topography (e.g. Doornbos & Hilton 1989; Souriau & Poupinet 1991; Rodgers & Wahr 1993; Obayashi & Fukao 1997; Garcia & Souriau 2000; Sze & van der Hilst 2003; Restivo & Helffrich 2006; Tanaka 2010; Schlaphorst *et al.* 2016).

To assess the effects of topography and 3-D velocity variations on the traveltimes, we perform a comparison between ray theory based predictions of time anomalies and cross-correlation time shift measurements measured on spectral-element synthetics. The latter are caused by only varying Earth models during our spectral-element simulations, that is adding CMB topography and/or 3-D velocity models.

The time shift measurements made on the spectral-element synthetic waveforms are considered as realistic representations of those made on real data. The traveltime comparisons are done similar to (Bai *et al.* 2012) and (Koroni & Trampert 2016). This type of comparison can provide insights into the reliability of traveltimes of the selected phases when interpreted within a linearized ray theoretical framework.

Second, we compute and demonstrate sensitivity kernels which show the finite frequency effects due to volumetric as well as boundary variations in the whole mantle and along CMB. Our motivation is to thoroughly assess the usability of such sensitivity kernels and their explicit contribution for determining CMB topography. For future iterative optimization of existing mantle velocity and CMB topography models, a targeted FWI workflow is essential in order to achieve higher resolution seismic imaging and efficiently use observable quantities from real data. This can be achieved with higher accuracy only when the finite frequency sensitivity is analysed and understood using adjoint sensitivity kernels. Our studies are performed based on well-established techniques using spectral-element waveform modelling and adjoint methods for calculating the Fréchet sensitivity kernels (e.g. Komatitsch & Tromp 1999, 2002a, b; Dahlen 2005; Tromp *et al.* 2005)

The paper is structured as follows: We first present the methods for carrying out the traveltime analyses and comparisons. Then, we explain the specifics of Fréchet sensitivity analysis and kernel computation using SPECFEM3D_GLOBE. Our results are presented for the two separate types of analyses, that is traveltime comparisons and sensitivity kernels. We afterwards discuss the results by using the finite frequency kernels to explain the comparisons between ray theory and cross-correlation time shift measurement.

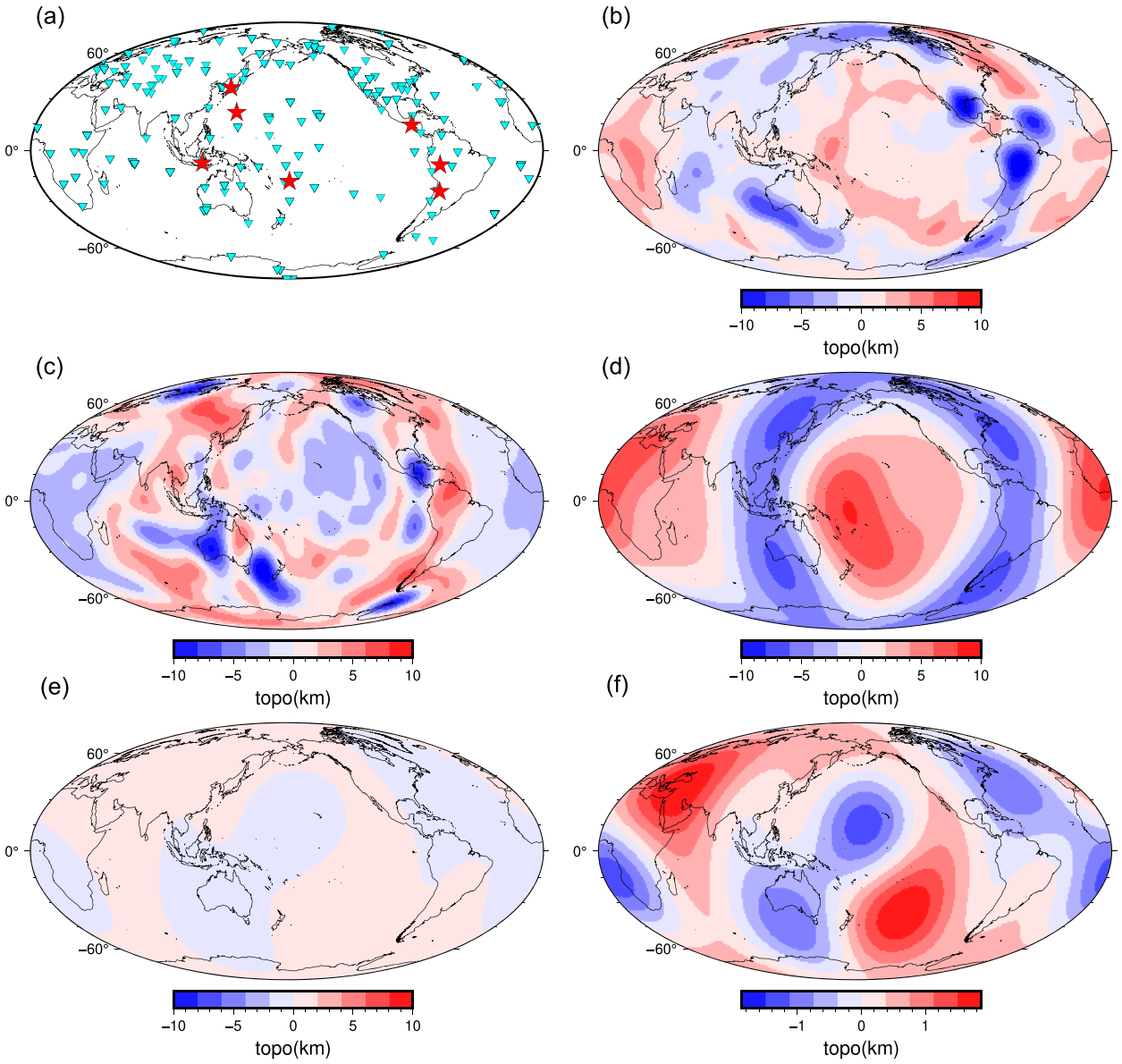

Figure 2. Maps of experimental set-up with synthetic earthquake events and stations used in this study (upper left) to create a realistic source–receiver configuration for our synthetic waveform simulations. Maps of the CMB topography models used in this study are shown in subplots (b) and (c). Specifically, panel (a) shows the events (red stars) and stations from the Global Seismographic Network (cyan inverted triangles). Panels (b)–(e) show models *T1* (b) and *TC1* (c) based on the mantle convection simulations of Deschamps *et al.* (2018; see the main text), and *LM91* (Li *et al.* 1991) (d) and *TK10* (Tanaka 2010) (e), inferred from real data. Panel (f) shows the same model *TK10* as in panel (e), except for this time there is a change in scale of the colour bar, as this model's topographic variations are much smaller than the other models.

2 METHODOLOGY

2.1 Computation of synthetic seismograms

In order to enhance our knowledge about CMB structure by investigating its effects on *P*- and *S*-seismic phases, we perform full-waveform modelling and focus on frequencies ranging from 0.01 to 0.08 Hz. This frequency range is due to the current computational limitations for higher frequency simulations. The theoretical ray paths of the chosen seismic phases are shown in Fig. 1, which is produced using 1-D ray tracing with tauP (Crotwell *et al.* 1999) and using model PREM as reference (Dziewoński & Anderson 1981).

The computation of synthetic waveforms is done using the open-source software package SPECFEM3D_GLOBE (Komatitsch & Tromp 2002a, b) in 1-D, that is PREM (Dziewoński & Anderson 1981), and 3-D mantle velocity models, that is S20RTS (Ritsema & van Heijst 2002) plus CRUST2.0 (Bassin *et al.* 2000). The synthetic waveforms are used to imitate realistic waveforms for the comparisons between ray theory and measurements and to assess the direct effects of CMB topography and 3-D velocity variations on the traveltime of the seismic phases.

For the comparisons of traveltimes, existing CMB topography models are added resulting in PREM or S20RTS plus CMB topography. We used four topography models in total, in order to examine the effects of a variety of topographies with larger peak-to-peak perturbations. A model with very low topographic variations, of the order of ±1 km, is used. This was derived by Tanaka (2010) using

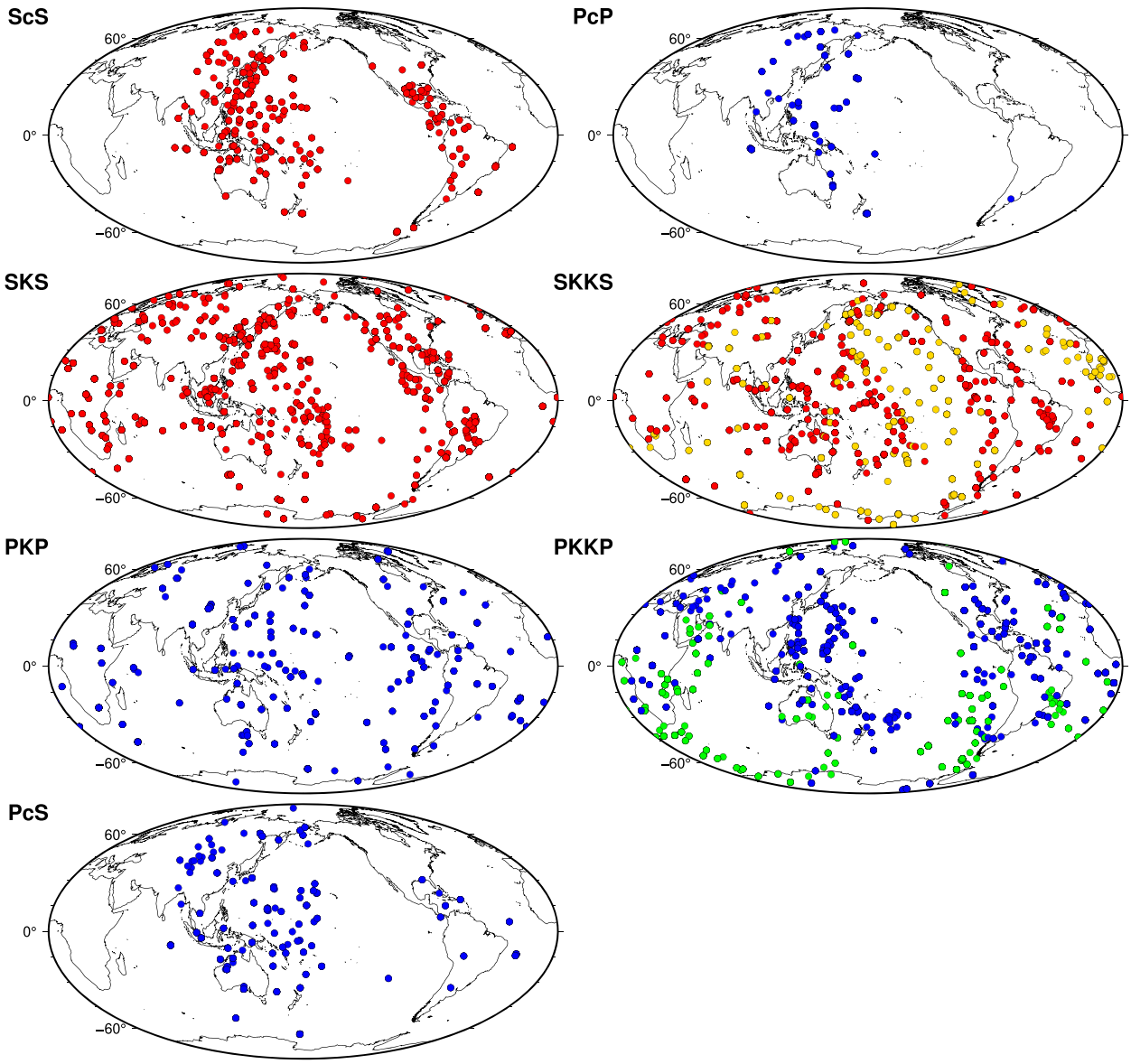

Figure 3. Bouncing or crossing points at the CMB for the seven seismic phases used in this study, as labeled in each panel. Blue-filled circles show *P* phases, while red circles show *S* phases. For *SKKS* and *PKKP*, yellow- and green-filled circles show the underneath bouncing points at the CMB.

differential traveltimes between *P4KP-PcP*. It is referred to here as *TK*. We also compute synthetic waveforms by adding the models by (Li *et al.* 1991) derived using Earth's free oscillations, denoted here as *LM91*, with peak-to-peak variation scaled up to 8 km. Additionally, two topography models derived from geodynamic simulations *T1-pPv* and *TC1-pPv* from (Deschamps *et al.* 2018), denoted here as *T1* and *TC1* for simplicity, with peak-to-peak variations reaching ±20 km are used. The two latter models are derived using thermal and thermochemical variations, respectively, in geodynamic modelling simulations. During these geodynamic simulations, density variations are incorporated in order to properly account for thermo-chemical effects.

In order to make the geodynamics models more applicable to our source–receiver geometry, model *TC1* is rotated so that its spherical harmonic degree-2 pattern match best that of S20RTS *S*-velocity variations right above the CMB (this is done by performing a simple grid search). The same is done for model *T1*, but with the sign of *S*-velocity variations inverted. This is because *S*-velocity anomalies at the CMB, and CMB topography variations are expected to be positively correlated for thermo-chemical models (*TC1*), but negatively correlated for purely thermal models (*T1*) (Deschamps *et al.* 2018).

Most of their peak-to-peak amplitude is however accommodated by deep depressions caused by downwellings reaching the CMB, while positive topography associated with plume clusters in *T1* and depressions associated with thermochemical piles in *TC1* have height or depth, respectively, of about 2km.

Using various possible topography models allows us to investigate the reliability of ray theoretical methods in a more conclusive manner. All CMB topography models used here along with the synthetic data set constructed by locating earthquakes and stations in order to obtain the desired source–receiver geometries and numerically simulate the selected earthquakes listed in Table 1 are displayed in Fig. 2. It should be kept in mind that we have not used real data from the listed earthquakes, rather we have used these events and station locations to create an experimental set-up

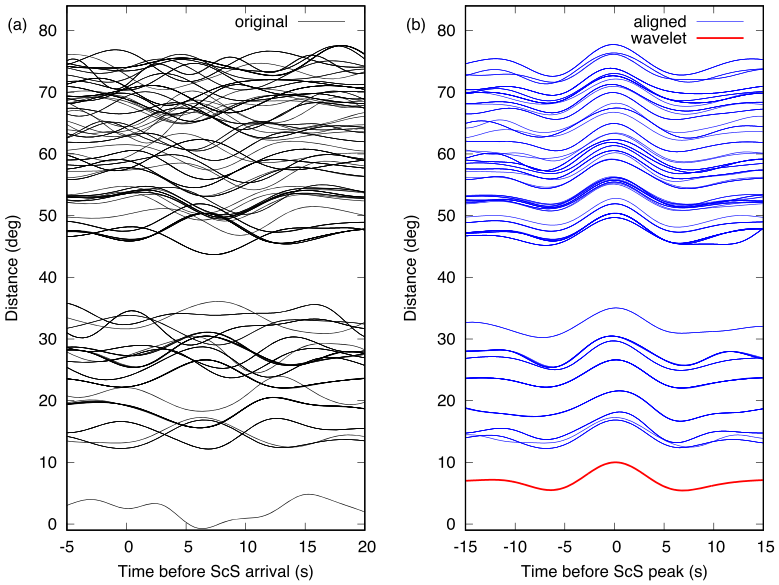

Figure 4. Illustration of the adaptive stacking procedure (Rawlinson & Kennett 2004) used to define the time windows, for the *ScS* phase for model S20RTS and event no. 1 in Table 1. (a) Waveforms before alignment, using time windows 5 s before, and 20 s after the *ScS* arrival; (b) same as (a), but after alignment using the source wavelet (red trace) obtained from the adaptive stacking procedure. As in the actual data selection procedure, traces with a correlation lower than 0.95 with the source wavelets are excluded from (b).

Table 1. Main features of the synthetic earthquake events used in this study. These are recorded at the station locations of the Global Seismographic Network.

Event no.	GCMT ID	Event location	M_w	Latitude (°)	Longitude (°)	Depth (km)	STF duration (*s*)
1	200609090413A	Flores Sea	6.3	-7.23	120.27	583.2	6.8
2	200707161417A	Sea of Japan	6.8	36.84	135.03	374.9	12.4
3	200709281338A	Volcano Islands (JP)	7.4	21.94	143.07	275.8	26.4
4	201409241116A	Jujuy Province (AR)	6.2	-23.78	-66.72	227.6	6.4
5	201303252302A	Guatemala	6.2	14.62	-90.71	186.4	6.2
6	200602021248A	Fiji Islands	5.9	-17.7	-178.13	611.6	11
7	101202H	Western Brazil	6.9	-8.30	-71.66	539.4	13.2

Table 2. Number of time windows used in this study for each phase before selection based on cross-correlation coefficients and after selection for the PREM and S20RTS models. Note the smaller number of *PcP* time windows before selection compared to *ScS*, which is in part due to *P* merging with *PcP* at smaller epicentral distances than for *S* and *ScS*.

Phase	Before selection	Selected (PREM)	Selected (S20RTS)
ScS	1273	795	550
SKS	2262	932	905
SKKS	2296	587	666
PcP	570	137	151
PKP	375	322	264
PKKP	1715	700	775
PcS	889	449	379

and compute corresponding synthetic seismograms to resemble a realistic study.

For the simulations, we set the resolution such that the resulting noise-free waveforms have minimum resolvable period of about $T = 11$ s. Some modelling parameters which are present in real data can be important, such as attenuation, and can have complex effects on traveltimes of seismic phases, thus they are not considered for our simulations, since we would like to focus on the effects of CMB topography and 3-D lateral isotropic variations without further complicating the waveforms.

It should be mentioned that attenuation is a critical property of Earth structure that further complicates interpretation and inversion of real data and should properly be taken into account in real data applications. In the finite frequency traveltime kernels shown in the remainder of this paper, attenuation is not expected to have a significant impact on the intermediate frequency traveltime sensitivity, that is not likely to change the appearance of the kernel significantly. However, it should also be mentioned that for the case of comparing real to synthetic waveforms for further inverting using the adjoint sensitivity kernels, full attenuation should be switched on during

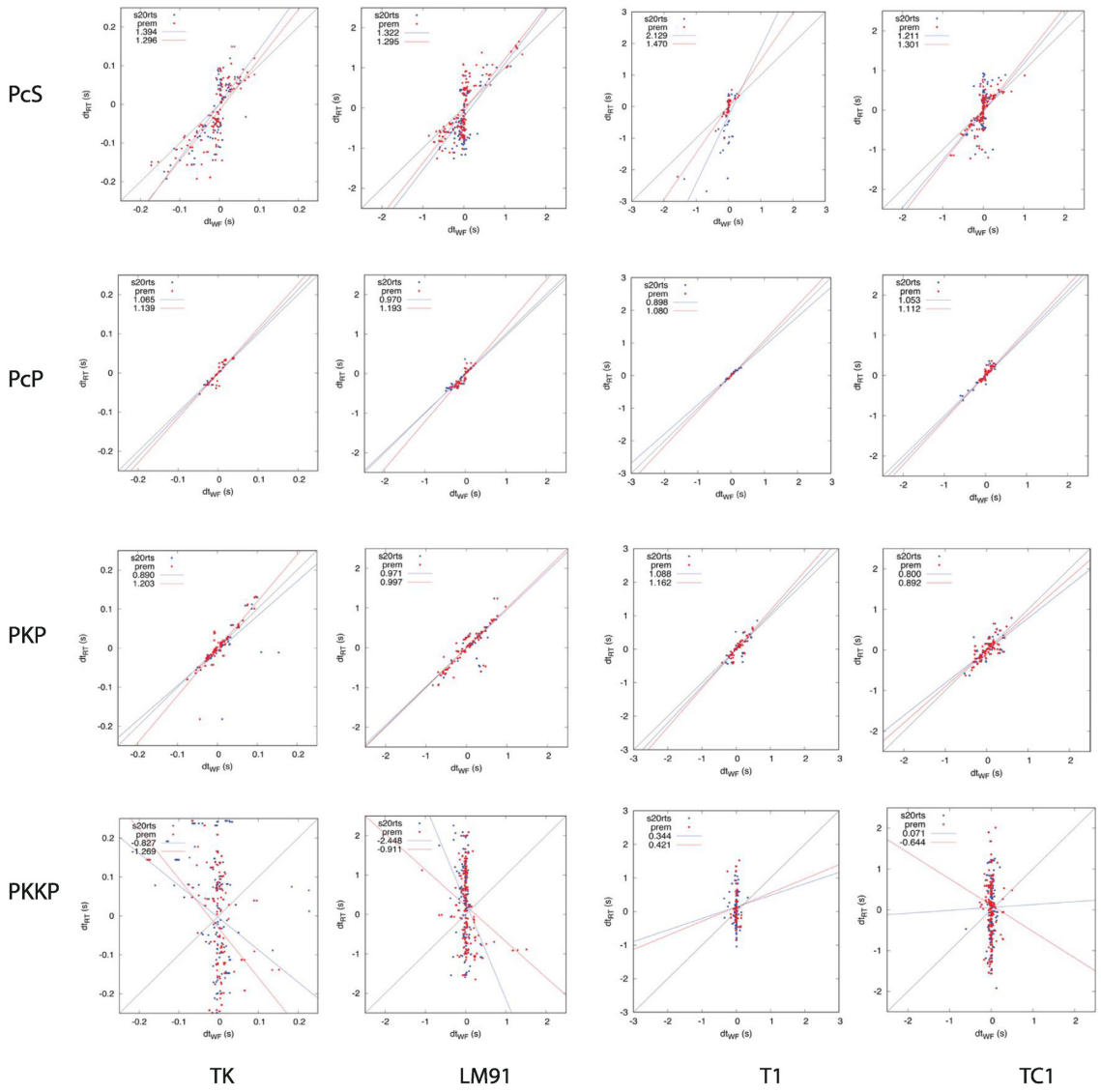

Figure 5. Comparison between ray theoretical prediction of time shift given a CMB topography model to the time anomaly measured on each time windowed seismic phase by comparing synthetic waveforms in 1-D and 3-D velocity background, red and blue points on the plots, respectively. Each column corresponds to a different topography model (*TK, LM91, T1, TC1*). Each row corresponds to a seismic phase (*PcS, PcP, PKP* and *PKKP*). Most of the phases show acceptable correspondence between predicted and measured by cross-correlation time shift, implying that the signature of CMB topography can be only partially captured by using RT. This is not the case for phase *PKKP*, where a prediction is worse and the time window isolation is insufficient to make a reliable measurement.

forward and adjoint simulations using SPECFEM3D_GLOBE since the effects of considering physical dispersion only can be significant (Komatitsch *et al.* 2016).

In order to create synthetic waveforms which best resemble a realistic data set, we use seven events with a range of focal depths, source time function duration and moment magnitudes in the range $M_w = 5.5$–7.5. The events are summarized in Table 1. The receiver locations are set to those of the Global Seismographic Network and we make measurements for each source–receiver pair as well as ray theoretical predictions, given the known topographic variation derived from the CMB models we use, for the same pairs. This is done in time windows around the seismic phases of interest. The synthetic data are processed by filtering using a bandpass between the frequencies 0.01–0.08 Hz. The synthetic waveforms are used for two different purposes: first, for comparisons of traveltime shifts caused by topographic variations in 1-D or 3-D mantle structure models and, second, for computing the sensitivity kernels for selected time windows encapsulating the maximum peak of the energy of our selected seismic phases.

It should be highlighted that event number 3 in Table 1 has a duration which is much larger than the resolvable period in our synthetics ($T \approx 11$ s and event duration STF ≈ 26.4 s). This would be omitted in a real data application. We however keep this event for the traveltime comparisons, as it allows us to have a better data coverage by including more source–receiver paths.

2.2 Comparison of ray theoretical time shift prediction and cross-correlation measurements

In this section, we describe the prediction of traveltime anomalies due to perturbations of CMB topography using ray theory (RT) and as measured on full-waveform synthetics computed using the spectral-element method (denoted by

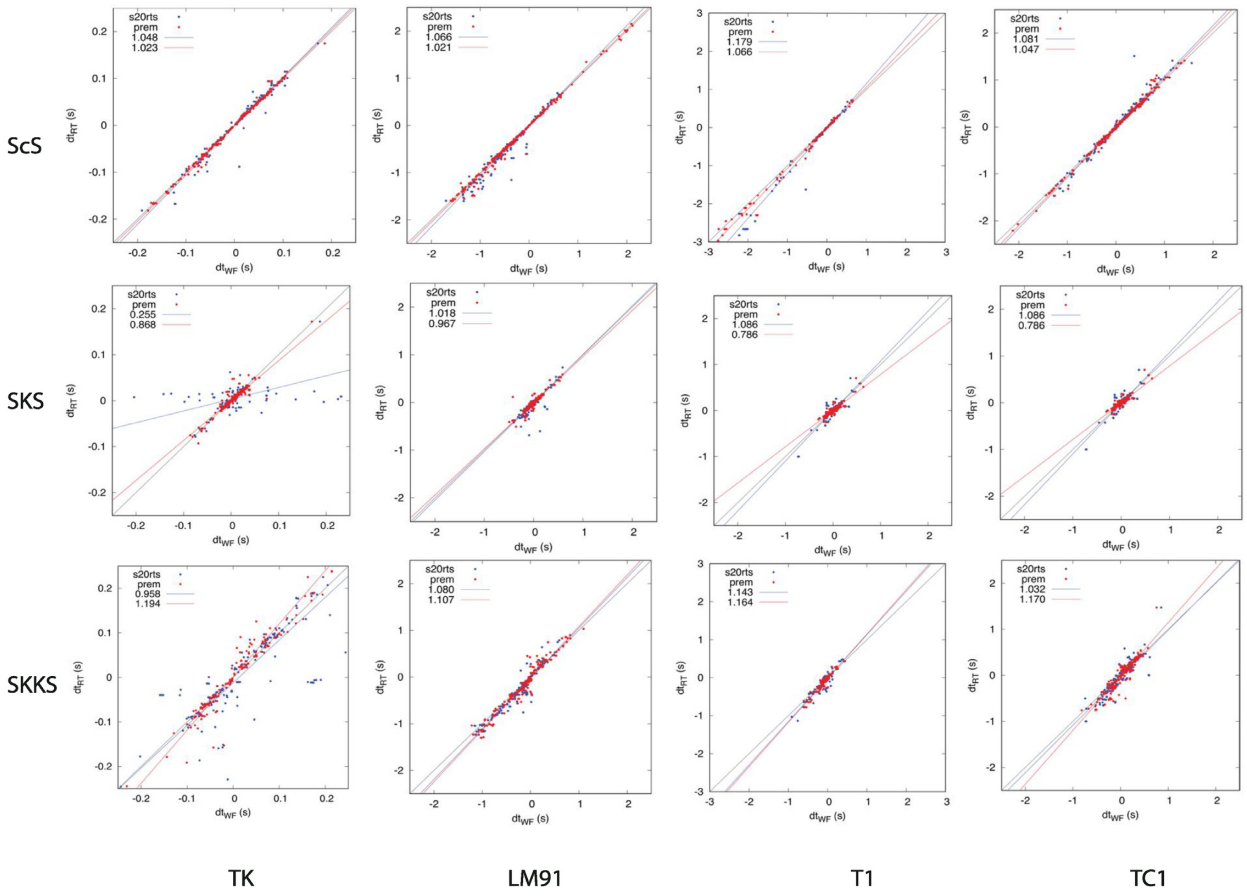

Figure 6. Similar as Fig. 5. Each row corresponds to a seismic phase (*ScS, SKS* and *SKKS*). Most of the phases show better correspondence between predicted and measured by cross-correlation time shift, implying that *S*-wave phases have a better sensitivity to CMB topography and this can be accommodated by RT.

Table 3. Slopes of the linear regression lines for the dt_{RT} versus dt_{WF} diagrams in Figs 5 and 6. Each cell shows two slopes, which correspond to S20RTS (left side of the forward slash) and PREM (right side) as a background model, respectively.

Phase	T1	TC1	TK10	LM91
ScS	1.18/1.07	1.08/1.05	1.05/1.02	1.07/1.02
SKS	0.88/0.79	1.09/0.79	0.26/0.87	1.02/0.97
SKKS	1.14/1.16	1.03/1.17	0.96/1.19	1.08/1.11
PcP	0.90/1.08	1.05/1.11	1.06/1.14	0.97/1.19
PKP	1.09/1.16	0.80/0.89	0.89/1.20	0.97/1.00
PKKP	0.34/0.42	0.07/-0.64	-0.83/-1.27	-2.45/-0.91
PcS	2.13/1.47	1.21/1.30	1.39/1.30	1.32/1.29

FW, which stands for full-waveform) using cross-correlation. The motivation for this analysis is to examine whether we can reliably predict a topographic perturbation given the ray-theoretical framework in a fixed background velocity model.

If this is true, the time shift as measured by cross-correlation and the predicted time anomaly for a specific topographic variation should be identical. In the opposite case, where the two values diverge, there are two implications: first, the ray-theoretical framework is shown to be not fully suitable for translating a measured time shift to a topographic variation, that is there is information loss. Second, there may be velocity effects which are not adequately taken into account when using a linearized interpretation within a ray-theoretical approach.

Traveltime perturbations due to the CMB topography are computed in the framework of ray theory following Morelli & Dziewonski (1987) and Tanaka (2010) and using the expressions given in eq. (1) when the ray reflects off the CMB (e.g. *ScS*), and eq. (2) when the ray transmits through the CMB (e.g. *SKS*):

$$\delta t_{\mathrm{ref}} = \pm\frac{2}{r}\left(\eta_{\mp}^2 - p^2\right)^{\frac{1}{2}}\delta r, \tag{1}$$

$$\delta t_{\mathrm{tra}} = -\frac{1}{r}\left[\left(\eta_{+}^2 - p^2\right)^{\frac{1}{2}} - \left(\eta_{-}^2 - p^2\right)^{\frac{1}{2}}\right]\delta r. \tag{2}$$

In these expressions, δr (in km) denotes the variation of the CMB radius at the bouncing points, p (in s rad^{-1}) is the ray parameter for the 1-D model without perturbations of CMB topography, and $\eta = r_{\mathrm{cmb}}/v(r_{\mathrm{CMB}})$ (in s rad^{-1}) is the vertical ray parameter, with η_+

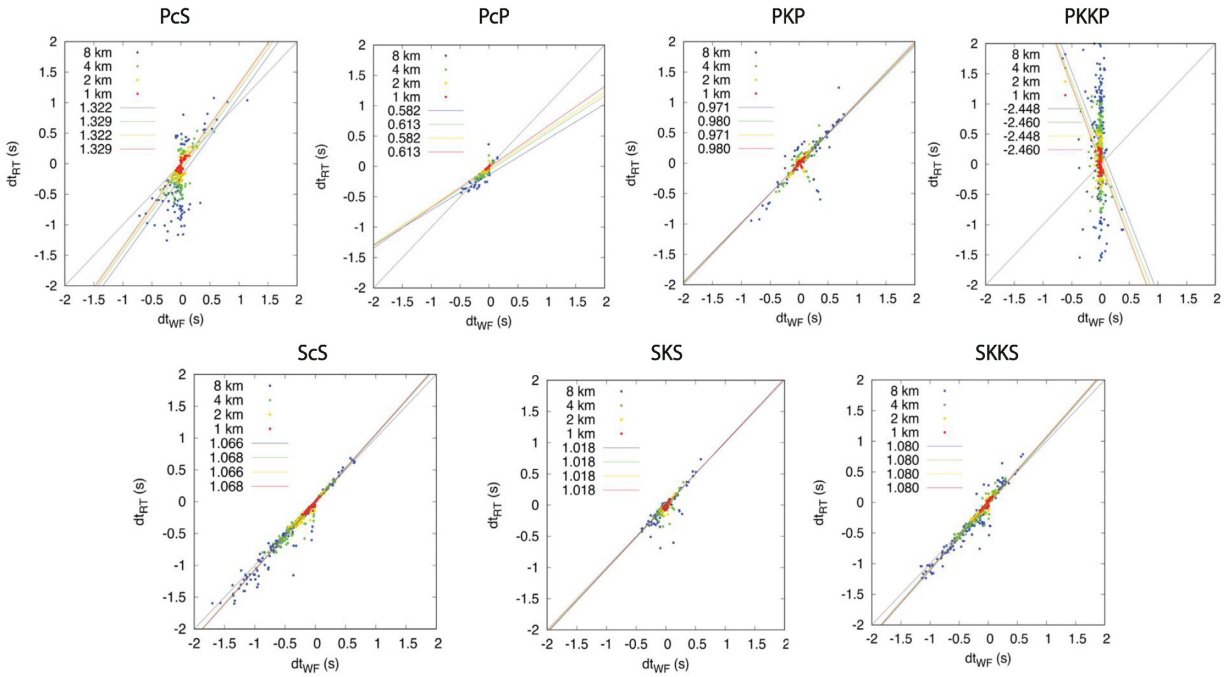

Figure 7. A test using four versions of the same topography model to check whether the amplitude of the variation linearly affects the RT prediction and cross-correlation time shift measurements. The model *LM91* is scaled for ±1 km (yellow dots), ±2 km (orange dots), ±4 km (green dots) and ±8 km (blue dots) topographic variations. The slopes of a simple linear regression for the cloud of points remain almost unchanged with the scaling of the model. This indicates that there is no clear dependence on the topographic variation when considering the agreement between prediction of RT and CC measurement.

and η_- representing the values of η just above and below the CMB, respectively.

In eq. (1), a positive sign is for underside reflection and a negative sign is for topside reflection. For PREM, which is our selected model, the values are: $\eta_+ = 479.03$ for *S* phases, $\eta_+ = 253.71$ for *P* phases, while $\eta_- = 431.51$, only *P* phases are supported in the core.

Measured traveltime perturbations are obtained by performing cross-correlation between synthetics for the reference model (either PREM or S20RTS) and for the same model with added perturbations of CMB topography. For each of the seismic phases *ScS, SKS, SKKS, PcP, PKP, PKKP* and *PcS*, we first compute preliminary time windows from 5 s before to 20 s after the arrival time of the phase as predicted using tauP (Crotwell *et al.* 1999) and PREM. We exclude time windows that overlap with the phases *S, SS, SSS, sS, P, pP, PP, PPP, sP* and *pS*, since overlapping phases affect the traveltime measurement by cross-correlation, which makes the comparison with ray theory less meaningful.

The time windows computed using tauP (Crotwell *et al.* 1999) are not adapted when the reference model is 3-D. We use the adaptive stacking algorithm of (Rawlinson & Kennett 2004) to compute time shifts to correct the time windows for the 3-D velocity structure. The algorithm proceeds iteratively as follows: (1) compute a source wavelet by stacking the waveform using the time windows from the previous step; (2) time-shift the time windows to maximize the cross-correlation with the source wavelet; (3) repeat with the improved time windows. The output of the adaptive stacking algorithm is the time windows aligned on their respective peak amplitude (corrected for time shifts due to 3-D velocity structure), and an average source wavelet.

Fig. 4 shows *ScS* waveforms for 3-D velocity model S20RTS using time windows computed computed with tauP (Crotwell *et al.* 1999) and after corrections using the adaptive stacking procedure. The inferred source wavelet is to discard anomalous time windows (i.e. with overlapping phases not predicted by TauP). The selection is done by imposing a minimum cross-correlation coefficient between a given time window, and the inferred source wavelet.

The final time windows have a length that ranges from −15 to +15 s after the arrival time of the peak for each phase. The purpose of adaptive stacking is only to define optimal time windows around the seismic phases to perform time-shift measurements in an improved way and to discard anomalous waveforms.

In the remainder of this section, the minimum cross-correlation coefficient is set to 0.8 for the *P* phases (*PcP, PKP, PKKP* and *PcS*) and to 0.95 for the *S* phases (*ScS, SKS, SKKS*), due the better isolation of *S* phases than for *P* phases. For the *PcP* phase, we further exclude all records at epicentral distances smaller than 40°, since such records show consistent, large disagreement between RT and FW. The total number of time windows before and after selection is shown in Table 2. The amount of time windows that satisfy our quality criteria becomes significantly smaller; however, we prefer to base our conclusion on a more robust data set of time shift measurements. The smaller numbers of high correlation coefficient time windows in noise-free synthetics also shows that the isolation of these phases can be considerably cumbersome in real data sets.

2.3 Computation of Fréchet sensitivity kernels

The sensitivity kernels are computed for time windows with a length of 30 s, which are centered on the predicted peak arrival of the *P*- and *S*-wave phases. The sensitivity is computed based on the Born approximation (e.g. Marquering *et al.* 1999; Dahlen *et al.* 2000; Dahlen 2005) and using adjoint methods as implemented in the software package SPECFEM3D_GLOBE for boundary (Dahlen 2005; Liu & Tromp 2008) and volumetric kernels (Tromp *et al.* 2005). With this analysis, we conduct an investigation of the traveltimes by

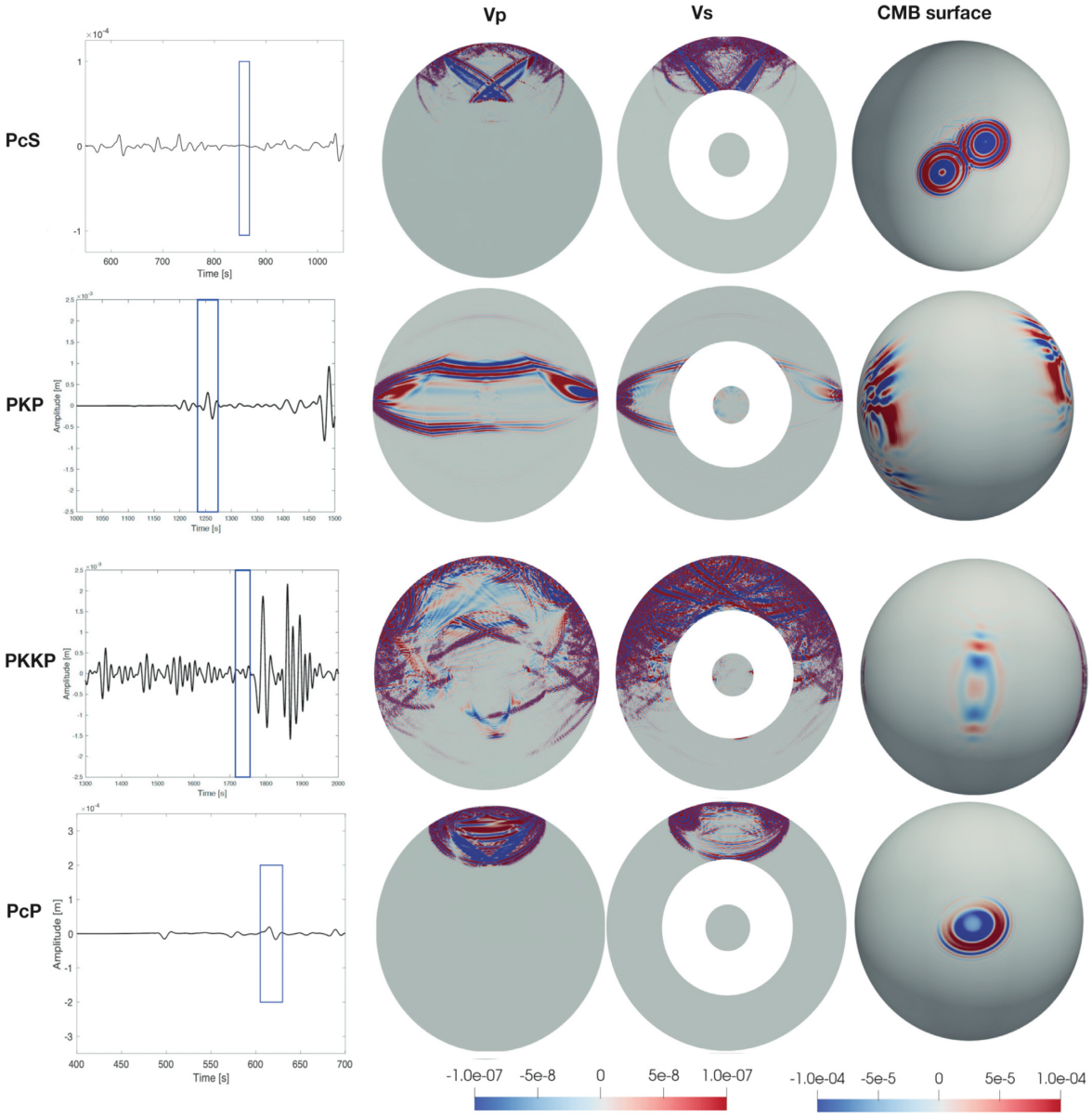

Figure 8. Fréchet sensitivity kernels for the group of *P* waves examined here. Each row corresponds to a phase, from left to right, the figures show: synthetic seismogram and corresponding time window isolating each phase, compressional wave speed volumetric kernel (V_P), shear wave speed volumetric kernel (V_S), boundary kernel with respect to the core-mantle interface. From top to bottom: *PcS* (53°), on radial component, PKP (160°), PKKP (110°), PcP (53°), all on the vertical component.
. The units of volumetric kernels are km^{-3} s and for the boundary kernels km^{-2} s.

visualizing their sensitivity to volumetric, i.e. shear and compressional wave speed mantle structure, and boundary parameters, that is the interface denoted as the CMB.

By computing these kernels our purpose is threefold. First, we visualize the traveltime sensitivity to the aforementioned parameters to provide a guide for the natural finite-frequency sensitivity and observe possible wave phenomena that will allow us to understand the traveltimes better. Second, we use these kernels to explain the observations from traveltime comparisons. Third, we assess the usability of the traveltimes of these seismic phases according to their visualized sensitivity to the boundary.

The kernels are computed with respect to the CMB radius and compressional and shear wave speed in 1-D background model, that is PREM. We compute the banana-doughnut traveltime kernels (e.g. Luo & Schuster 1991; Marquering *et al.* 1999; Dahlen *et al.* 2000), which associate a traveltime measurement on the waveforms to the changes in finite frequency sensitivity with respect to the chosen background model. The relationship connecting a traveltime window to volumetric structure defined by seismic properties of compressional (α) and shear (β) wave speed are shown below.

The following expressions are given for a reference seismic receiver r at position x_r. The reader is referred to the work of Tromp *et al.* (2005) for the complete derivations using the adjoint method. The volumetric kernels are related to the time window via:

$$\delta T_r = \int_V K_{\alpha,\beta}(\mathbf{x}, \mathbf{x_r}) \delta \ln \alpha, \beta(\mathbf{x}) \mathrm{d}^3\mathbf{x}, \tag{3}$$

The units of volumetric wave speed kernels are s km^{-3}.

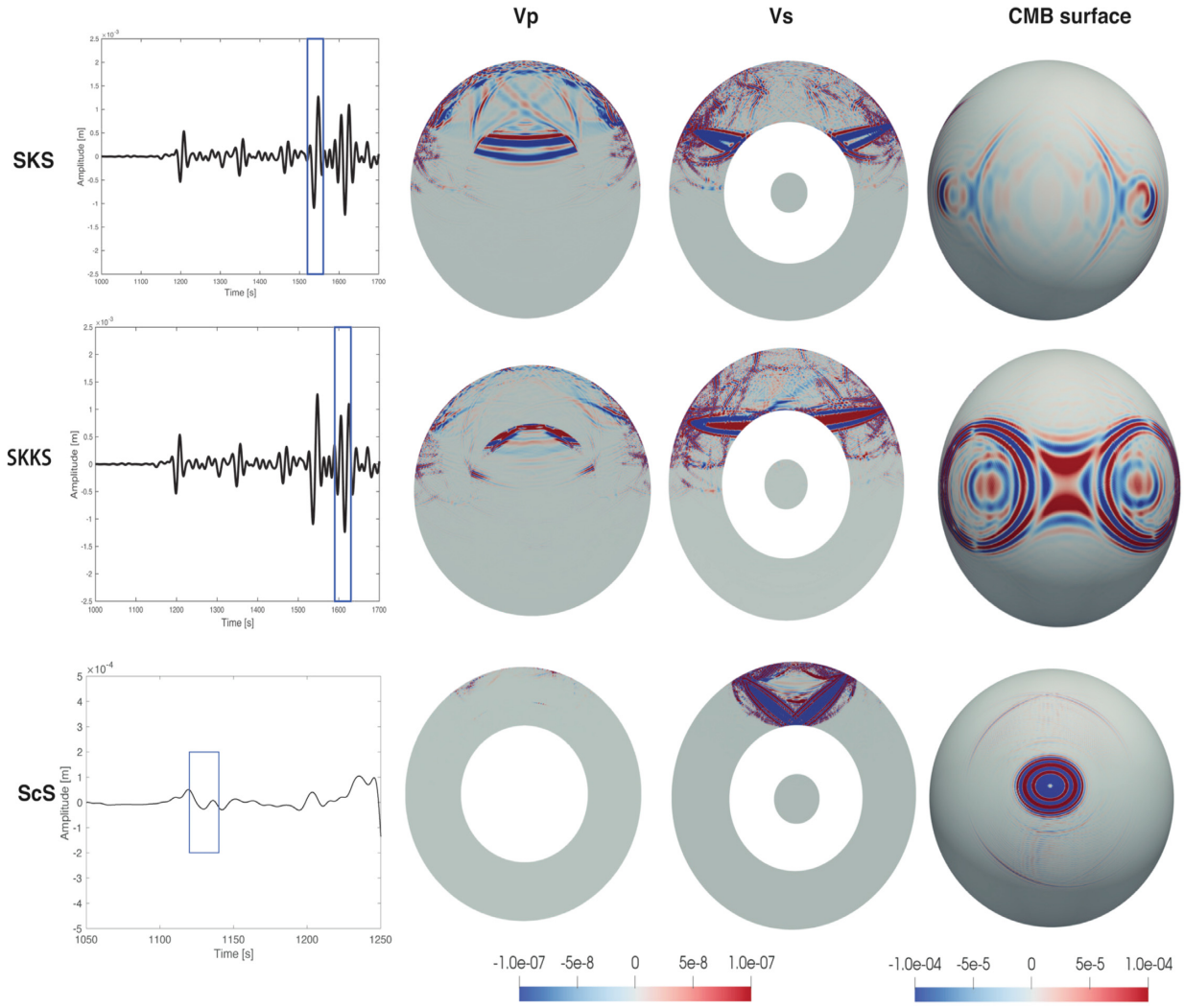

Figure 9. Similar to Fig. 8, now for the selected *S*-wave phases. From top to bottom: SKS (117°), SKKS(117°), on the radial component of displacement seismogram, and *ScS* (53°), on the transverse component. The units of volumetric kernels are km^{-3} s and for the boundary kernels km^{-2} s.

The expression relating the traveltime window which encloses the seismic phase to the boundary perturbation of the radius to the CMB (solid–fluid interface denoted by ΣSF) is based on the theory derived by Dahlen (2005) and implemented in the spectral-element method by (Tromp *et al.* 2005):

$$\delta T_r = \int_{\Sigma SF} \mathbf{K}_h \cdot \delta h(\mathbf{x}) \mathrm{d}^2\mathbf{x}, \tag{4}$$

whereby $\mathbf{K_h}$ is the time integration for variations along the boundary (Dahlen 2005). The units of boundary kernels are s km^{-2}.

We select the phases for a set-up of source–receiver that is appropriate for isolating them adequately and avoiding major interference of phases arriving at similar times (e.g. refer to Fig. 1, left side). The source receiver geometries are selected also based on their commonly observed epicentral distance. All time windows are selected on displacement seismograms.

We have set the source time function to be 6 s long and the focal depth of the earthquake event is set to 20 km. A deeper earthquake event would allow the peaks of these phases to be better separated and also see less pronounced topside reflections. However, having a shallower event depth allows us to visualize the kernels with more symmetric legs with respect to the bouncing points of the seismic phases paths.

For the seismic phases *ScS, PcP* and *PcS,* the epicentral distance is chosen to be 53° on transverse (*ScS*) and vertical/radial components (*PcP/PcS*). The specific epicentral distances are chosen so that the phases are less likely to interact with *SS, PP* and *P*, respectively. The phases *PKKP, SKS* and *SKKS* are observed at an epicentral distance equal to 117° for better isolation of their theoretical arrival time and to avoid interference with the *SPdKS* seismic phase (Thorne & Garnero 2004). These are selected on vertical (*PKKP*) and radial (*SKS, SKKS*) components of displacement seismograms. The *PKP* phase is selected on the vertical component at a distance of 160° as, according to 1-D ray theory and tauP analysis, it is better separated from the *PKIKP* phase at this distance. The traveltime curves are shown in Fig. 1 with annotated characteristic distances for each seismic phase window.

For the visualization of the sensitivity kernels, we use a characteristic scale length, which is appropriate for the range of data values of the kernels and allows us to observe the theoretical finite frequency sensitivity.

After combining the kernel files for each volumetric region (mantle and core) and for the CMB interface, the kernels are visualized

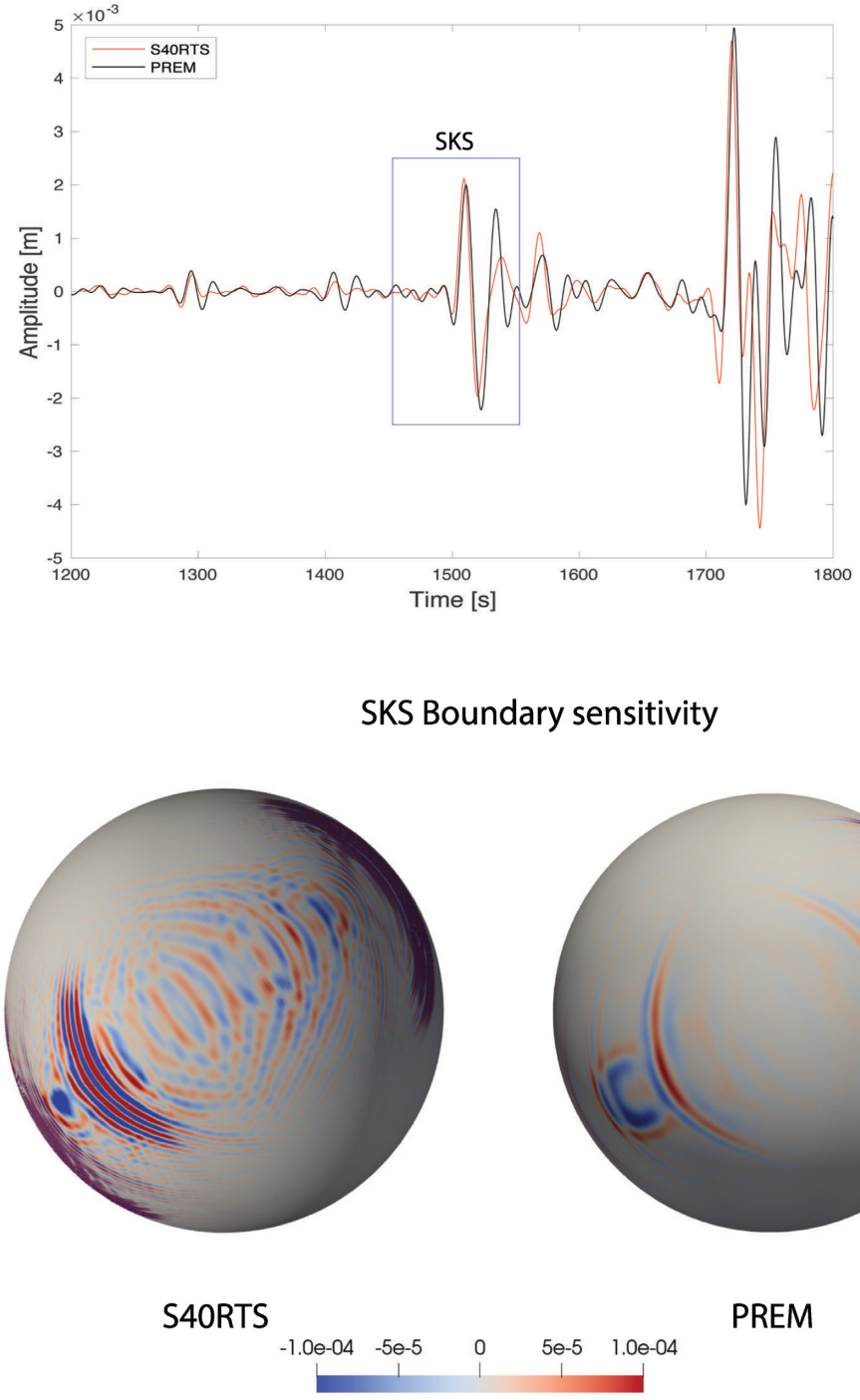

Figure 10. Comparison between the boundary kernels computed in 3-D background using model S40RTS (red line) and the same seismic phase *SKS* in 1-D background PREM (black line). The fact that the boundary kernels differ due to the different background model shows that interpretation of the traveltime shift of the phases due to topography should take into account the effect of 3-D velocity variation on the boundary sensitivity, ideally in a nonlinear way (not only by subtracting a time shift correction due to the 3-D mantle model). The units of boundary kernels are $km^{-2} \cdot s$.

using ParaView (Ayachit 2015). Considering the expressions given above, that is eqs (3) and (4), a direct comparison between boundary and volumetric kernels is not straightforward and perhaps not meaningful. It is however instructive to consider that the traveltimes of the selected seismic phases will likely show sensitivity to both parameters (volumetric and boundary), as expected due to the well-known trade-off between velocity and CMB structure, and thus it is worthwhile to separately judge the qualitative effects of volumetric and boundary structure.

3 RESULTS

3.1 Traveltime analysis using full-waveform synthetics

In this section, we show the comparisons of traveltime anomalies measured on FW synthetics to RT prediction for phases *ScS, SKS, SKKS, PcP, PKP, PKKP* and *PcS*. In Figs 5 and 6, we present the results of this comparison for all topography models and for all selected phases, for synthetic waveforms calculated using PREM

and S20RTS (1-D and 3-D, respectively) as velocity background models.

In these figures the predicted by RT and measured on FW time shift due to a topographic variation, caused by the various CMB topography models, for each bounce point shown in Fig. 3 are plotted against each other in scatter plots. The red points correspond to a 1-D background model, i.e. PREM, whereas the blue points are for a 3-D background velocity model, i.e. S20RTS. We also perform a linear regression which produces a regression line for each of model. The slope value is shown on the top left of each subplot.

If the prediction using RT and a known topographic variation at each bounce point could accurately explain the traveltime shifts for each of these seismic phases, all points in Figs 5 and 6 would lie on a line with a slope equal to one. However, the slopes of the linear regression lines have values slightly different from one, as summarized in Table 3.

For the *ScS* phase (which gives the most corresponding results between RT predictions and FW measurements) with PREM as a background model, deviations from a perfect agreement are between 2 per cent to 7 per cent, while other well-resolved phases (*SKS, SKKS, PcP* and *PKP*) show deviations of up to 26 per cent (for the *SKS* phase for model *T1*). This is true when the background velocity model is identical between the compared waveforms and by adding only a CMB topography model. In this case, we use PREM which is a 1-D model and is also consistent with the ray theoretical predictions made for the given topography model.

Figs 5 and 6 show that there is part of the measured traveltime shift which is not fully recovered when translating a topographic variation to time delay using ray theory. This means that the ray theoretical expression cannot fully explain the topographic variation as time anomaly measured in full-waveforms with and without topography perturbation. It seems to also vary with different topographic models and for each of the phases.

Figs 5 and 6 show that the agreement between a ray theoretical prediction of time anomaly caused by topography and the equivalent measurement on full-waveform synthetics is better for *S*-wave phases than for *P*-wave phases. More specifically, *ScS, SKS, SKKS* (and *PKP* from the *P* waves) traveltime shifts due to topography seem to be better predictable with ray theory. However, it should be noted that the difficulty in predicting an adequate time anomaly may not be solely due to ray theoretical limitations. Additional difficulties may also arise when trying to isolate the *P*-waves.

This is particularly true for the *PKKP* phase, where the slopes show a great deviation from a slope equal to one. It is also shown that sometimes they exhibit negative slopes, which is indicative of not predicting uplift or depression of CMB correctly. This is a likely indication that at the particular frequency range used in this study, this phase is not well isolated due to unclear peaks which probably include its various branches. Nonetheless, as seen in the finite frequency kernels below, its sensitivity to CMB is non-zero, meaning that in a FWI workflow the measurements done in similar time windows around the predicted *PKKP* arrival can contribute to the misfit function.

Focusing on the comparisons on S20RTS as a background model (blue dots on Figs 5 and 6), we observe that the agreement between RT and FW worsens compared to PREM in the background. Table 3 summarizes the slope values. There we can notice that for the *ScS* phase deviations from a perfect agreement between RT and FW are ∼1.6 to ∼3.5 times larger (i.e. 5–8 per cent) for S20RTS as a background model than for PREM depending on the topographic model. The slopes vary with the topographic model and seem to increase for models with larger absolute peak-to-peak topographic variations, albeit not significantly.

We further investigated this behaviour by computing traveltime residuals for three scaled versions of model *LM91*, with maximum topographic amplitudes of: ±1, ±2 and ±4 km, in addition to the original version of model *LM91*, whose maximum peak-to-peak amplitude is ±8 km. These are shown in Fig. 7.

The results for a 3-D background show that the slope values are very close for all the scaled versions and the original model. It is also noticed that the slopes are almost unchanged for *S*-phases. The very slight change in slope implies that the amplitude of the topography has some effect, but it does not crucially affect the agreement between RT and FW, at least for amplitudes ranging from ±1–8 km, which is approximately the range of amplitudes found by past studies.

We can assume that the traveltime shifts for these seismic phases are not highly sensitive to a change in absolute topographic variation from ±1 to ±8 km. It is also perhaps fair to assume that for the particular frequency content, a traveltime shift measurement and given a correction for a known velocity background model (here measurements are done for a fixed background model) may not be able to discern a larger from a smaller topographic variation.

We note that S20RTS is a relatively smooth 3-D model compared to more recent global tomographic models. We expect even larger discrepancies for 3-D models with stronger, smaller-scale velocity anomalies [e.g. S40RTS (Ritsema *et al.* 2011) or SEMUCB-WM1 (French & Romanowicz 2014)].

Our results illustrate the key role played by 3-D velocity variations in determining traveltimes. The result indicates that the measurements on full-waveform synthetics show discrepancies with ray theoretical predictions. This holds even though the measurement is done by comparing 3-D and 3-D+CMBtopo synthetics (keeping the velocity model unchanged).

This shows the highly nonlinear effects of topography and 3-D variations on traveltimes of these phases, when topography is the only parameter added to the simulation. It is expected that some of the difference could properly be accounted for when a 3-D velocity correction is made.

However, it is not expected that the correction will fully compensate the observed difference. As we show in the next section, this is due to nonlinear trade-off between CMB topography and the 3-D structure of the lowermost mantle and to finite frequency effects.

3.2 Fréchet kernels for CMB related phases

Fig. 8 shows the sensitivity of the *P*-wave phases under investigation. The Fréchet derivatives are computed for compressional (V_P) and shear wave speed (V_S) as well as for the interface denoting the CMB at approximately 2890 km for the chosen background model, i.e. PREM. All *P*-wave phases show their theoretical, finite frequency, hence broader, sensitivity to V_P. This indicates that the time window chosen around the predicted arrival according to PREM encapsulates the phases well and they present little to minimal interference with other major seismic phases.

It is worth noting that, specifically the *PcS* and *PcP* phases exhibit considerable sensitivity to shear wave speed. This indicates more complex mantle structure contributions to their traveltimes and perhaps explains the weakening of their sensitivity to topography, as shown in the analysis in Section 3.1. It should also be noted that *PcS* and *ScP* interfere in the same time window as we select it on the radial component. This is evident also on the V_P and V_S

kernels in Fig. 8 and it is a natural consequence given the window selection which however does not complicate our interpretation of the resulting finite frequency kernels.

Regarding the *S*-wave phases, displayed in Fig. 9, their traveltime sensitivity to shear and compressional wave speeds and CMB surface are shown in a similar way as for *P* waves in Fig. 8. It is readily observed that the shear wave speed kernels computed for the targeted time windows clearly show their theoretical path, in this case broader and more extended as expected from finite frequency theory.

The seismic phase *SKS* is characterized by a broad and noisy sensitivity. The theoretical paths of *SKS, SKKS* through the mantle are very similar, with their major differences appearing while travelling through the outer core. This is why their differential time has frequently been used for shear wave splitting studies in the lowermost mantle (e.g. Souriau & Poupinet 1991; Favier & Chevrot 2003; Restivo & Helffrich 2006; Sieminski *et al.* 2008). The *S*-wave phases also show clear contributions mainly from their theoretically predicted path. In contrast to the *P*-wave kernels, there is very low sensitivity of these phases to compressional wave speed.

Turning to the boundary kernels, from visual inspection it becomes apparent that contributions to the traveltime sensitivity are low, especially for the traveltime windows of *PKP* and *PKKP*. A low boundary sensitivity means that the traveltime will not be significantly affected due to the structure at the CMB. Hence, the particular seismic phase does not seem to arrive at a considerably different time than that reference traveltime prediction using PREM due to the interaction with the CMB and its topography, meaning minimal time shifts between observed and synthetic waveforms. This can explain the rather small change of the slope values when we vary the peak-to-peak topography shown in Fig. 7.

The boundary sensitivities of *PcS* and *PcP* are more pronounced. Considering the boundary sensitivity of *S* waves displayed in the kernels shown in Fig. 9, we observe that also for these phases, the reflected *ScS* phase has a clearer sensitivity to the CMB. However, for *SKS* and *SKKS*, as shown by their corresponding boundary kernels, most of the sensitivity is observed at the piercing points in and out of their way through the outer core, with *SKKS* showing a stronger contribution to its traveltime window due to boundary depth changes.

4 DISCUSSION

We have compared ray theoretical predictions of traveltime anomalies (RT) caused by CMB topography variations to measurements on full-waveform (FW) synthetics computed for models with and without CMB topography perturbations, similar to Bai *et al.* (2012) and Koroni & Trampert (2016). The comparisons were made both on 1-D and 3-D background velocity models. This allowed us to better comprehend the separate effects of structural and topographic parameters on traveltimes of commonly observed and routinely used seismic phases.

We complemented this analysis by computing finite frequency traveltime kernels (Marquering *et al.* 1999; Dahlen *et al.* 2000; Tromp *et al.* 2005) using the adjoint method. We then visualized the finite frequency effects of boundary and volumetric model parameters on traveltimes. We explicitly calculated boundary sensitivity kernels, which illustrate the influence of CMB interface variations on observed traveltimes.

Regarding the traveltime analyses, we find that for *P*-wave phases (Fig. 5) the agreement between RT and measurement on FW synthetics is lower than for *S*-wave phases (Fig. 6). This can be due to the following reason: It is generally expected that *P*-wave propagation is rather complex when interaction with strong velocity contrasts occurs (Doornbos & Mondt 1980; Aki & Richards 2002). This causes a separation of the incident *P* wave to both up- and downgoing *P* as well as *S* waves. When a *P*-wave interacts with the CMB interface, it loses significant energy, since it reflects and refracts as both *P* and *S* waves resulting to a weaker arrival on the recorded seismogram. A further consequence of that phase isolation using time windows is consequently more difficult for *P* waves.

This results in less prominent waveform peaks, at least when they are observed at intermediate frequencies as the ones in our study. Similar problems occur when trying to observe and make measurements on *PP* precursors (e.g. Lessing *et al.* 2015). In an analogous study, it was shown that the contribution of *PP* precursors to a narrow time window around their waveform peak is rather low and obscured by other, more prominent interfering phases (Koroni *et al.* 2019). In the study presented here, especially the *PKKP* phase is shown to be poorly isolated, with additional difficulties due to its multiple branches, which constitute phase isolation by time windowing rather complicated (Rost & Garnero 2004).

However, the finite frequency V_P kernels in Fig. 8 show that all *P*-phases have strong contributions to their predicted traveltime windows, while minor interference with other phases does not hinder a clear sensitivity to their theoretical path through the mantle and outer core. The V_S sensitivity of *P*-phases is shown to be equally significant (V_S kernels on Fig. 8). This corroborates our reasoning that more complex *P*-wave propagation leads to less reliable traveltime measurements when trying to isolate *P*- phases, at the frequency range between 0.01-0.08 Hz used in this study.

Regarding the *S*-phases, their traveltime sensitivity to shear wave speed indicates a clear influence of mantle structure. The theoretical paths are well indicated and insignificant wave interference from other seismic phases occurs. It is also observed that *S* waves are much less sensitive to compressional wave speed, compared to the observed shear wave speed structure sensitivity of *P*-phases under investigation.

The double sensitivity observation, that is *P* phases sensitivity to V_S and *S* phases to V_P, is important when considering a reliable translation from measured time shift to topography. If this is performed without accounting for the double sensitivity to V_P and V_S, it can lead to loss of accuracy when correcting for mantle structure using linearized ray theory. This is manifested by the volumetric velocity kernels with respect to both wave speed parameters and for all phases in Figs 8 and 9 which have mostly non-zero values. Loss of accuracy can occur because the corrections are usually done for a predicted time anomaly given a velocity model, V_P for *P*-phases and V_S for *S*-phases. Given the shown double sensitivity, traveltime corrections should therefore be considered with care.

The overall observations from the boundary kernels leads us to the inference that *PcP* and *PcS* are more sensitive to CMB interface, while *PKP* and *PKKP* are much less affected by its surface variations. Nonetheless, the imprint of topography is captured in the traveltime prediction and measurement. This can explain the relatively good correspondence between RT and FW shown in Figs 5 mainly for the *PKP* phase, although not for *PKKP*. This leads us to argue that *PKKP* is difficult to observe and make reliable traveltime measurements in its predicted time window, especially at this frequency range.

The traveltime analysis of *S*-waves shows overall great agreement between predicted and measured time anomalies (Fig. 6). By inspecting the boundary sensitivity kernels in Fig. 9 we can observe that indeed the phases *ScS* and *SKKS* exhibit considerable sensitivity to CMB structure, while the *SKS* is less affected.

By presenting these traveltime sensitivity kernels, we propose that most of the examined seismic phases are useful, because they show sensitivity to depth variation along the CMB as well as to the velocity structure in the mantle and core. Specifically, boundary sensitivity seems to be higher for CMB reflected phases, that is, *PcP, ScS, PcS* and for *PKP*. This corroborates the results from previous studies by Colombi *et al.* (2014), who successfully used these phases for CMB topography inference.

We further investigated whether larger peak-to-peak variations in topography can considerably affect time shifts, measured and predicted as well as their agreement. To achieve this, we ran tests for a scaled version of CMB topography models (Fig. 7). From these tests, we observed that the pattern of agreement between predicted and measured time shifts does not considerably vary with scaling peak-to-peak variations of CMB topography models. The slopes of linear regression remain close in values, thus showing that all peak-to-peak topography variations introduced for this test could produce similar time shifts. This can also be interpreted as a weaker effect of topography on traveltimes compared to mantle structure.

The well-reported trade-off between boundary and volumetric parameters (e.g. Tanimoto 1990; Cottaar & Romanowicz 2012), that is CMB topography and velocity, can be readily assessed in the example we provide in Fig. 10. We computed the boundary kernel for the same seismic phase. For exemplification we have chosen the *SKS* phase for a source–receiver distance equal to 110°. in different background models, namely 1-D (PREM) and 3-D [S40RTS Ritsema *et al.* (2011)]. The time window has been chosen around the predicted arrival of the given seismic phase. For each boundary kernel, the background model is the same as for the computation of the waveform for the selection of the time window. The boundary sensitivity is shown to be significantly altered when changing the mantle background velocity model. This means that the boundary and velocity effects are not directly separable and should be jointly considered. We propose that an FWI scheme is ideal for a joint inversion, as it can take into account the naturally occurring finite frequency sensitivity and consistently account for the intricate trade-off by using both boundary and volumetric kernels.

5 CONCLUDING REMARKS

From the analyses conducted in this study, we draw the following conclusions:

(i) It is easier to isolate *S* phases in narrow time windows compared to the *P* phases we examined and at this computationally feasible frequency range. A translation of time shifts measured on these windows can more reliably be done using a ray theoretical framework.

(ii) The seismic phases *PcP, ScS, PcS* and *SKKS* present high sensitivity to CMB interface variations and therefore they are useful for inversions using the boundary kernels shown in this study.

(iii) Sensitivity to both volumetric parameters, namely V_P and V_S, is prominent and should be accounted for when performing linearized traveltime corrections for mantle structure.

(iv) An FWI scheme for jointly inverting for lowermost mantle velocity structure and CMB topography is necessary, since these two parameters intricately affect traveltimes of frequently used seismic phases. As it was similarly shown for upper-mantle discontinuities (Koroni & Trampert 2021), using boundary kernels as computed with the adjoint method allows us to better resolve CMB structure with an inversion that is guided by the explicitly computed boundary kernels.

ACKNOWLEDGMENTS

We would like to thank the editor, Ebru Bozdağ, as well as Michael Thorne and an anonymous reviewer for their questions, comments and suggestions, which helped us to improve this manuscript. MK would like to thank Yorgos Efstathiou for carefully proofreading the manuscript and providing essential feedback. We used the open source community software SPECFEM3D_GLOBE and we would like to thank its developers. The source package can be found and freely downloaded from https://geodynamics.org/cig/software/specfem3d_globe/. Most of the plots are made using ParaView (Ayachit 2015) and ObsPy (Krischer *et al.* 2015). MK was supported by the European Union's Horizon 2020 - Research and Innovation Framework Programme (grant agreement 714069, CSEM).

DATA AVAILABILITY

The data underlying this paper will be shared on reasonable request to the corresponding author.

REFERENCES

Aki, K. & Richards, P.G., 2002. *Quantitative Seismology, Theory and Methods,* W. H. Freeman.

Amit, H., Deschamps, F. & Choblet, G., 2015. Numerical dynamos with outer boundary heat flux inferred from probabilistic tomography - consequences for latitudinal distribution of magnetic flux, *Geophys. J. Int.,* **203,** 840–855.

Ayachit, U., 2015. *The ParaView Guide: A Parallel Visualization Application,* Kitware.

Bai, L., Zhang, Y. & Ritsema, J., 2012. An analysis of *SS* precursors using spectral-element method seismograms, *Geophys. J. Int.,* **188,** 293–300.

Bassin, C., Laske, G. & Masters, G., 2000. The current limits of resolution for surface wave tomography in North America, *EOS,Trans. Am. geophys. Un.,* **81,** F897.

Becker, T.W. & Boschi, L., 2002. A comparison of tomographic and geodynamic mantle models, *Geochem. Geophys. Geosyst.,* **3**(1), https://doi.org/10.1029/2001GC000168.

Bloxham, J. & Jackson, A., 1992. Time-dependent mapping of the magnetic field at the core-mantle boundary, *J. geophys. Res.,* **97(B13),** 19 537–19 563.

Borgeaud, A. F.E., Kawai, K., Konishi, K. & Geller, R.J., 2017. Imaging paleoslabs in the D″ layer beneath Central America and the Caribbean using seismic waveform inversion, *Sci. Adv.,* **3**(11), doi:10.1126/sciadv.1602700.

Brown, S., Thorne, M., Miyagi, L. & Rost, S., 2015. A compositional origin to ultralow-velocity zones, *Geophys. Res. Lett.,* **42,** 1039–1045.

Calkins, M.A., Noir, J., Eldredge, J.D. & Aurnou, J.M., 2012. The effects of boundary topography on convection in Earth's core, *Geophys. J. Int.,* **189**(2), 799–814.

Cobden, L., Thomas, C. & Trampert, J., 2015. Seismic detection of post-perovskite inside the Earth, in *The Heterogeneous Mantle,* pp. 391–440, eds Khan, K. & Deschamps, F., Springer.

Colombi, A., Nissen-Meyer, T., Boschi, L. & Giardini, D., 2012. Seismic waveform sensitivity to global boundary topography, *Geophys. J. Int.,* **191**(2), 832–848.

Colombi, A., Nissen-meyer, T., Boschi, L. & Giardini, D., 2014. Seismic waveform inversion for core-mantle boundary topography, *Geophys. J. Int.,* **198,** 55–71.

Cottaar, S. & Romanowicz, B., 2012. An unsually large ULVz at the base of the mantle near Hawaii, *Earth planet. Sci. Lett.,* **355-356,** 213–222.
Creager, K.C. & Jordan, T.H., 1986. Aspherical structure of the core-mantle boundary from PKP travel times, *Geophys. Res. Lett.,* **13**(13), 1497–1500.
Crotwell, H.P., Owens, T.J. & Ritsema, J., 1999. The TauP toolkit: flexible seismic travel-time and raypath utilities, *Seismol. Res. Lett.,* **70,** 154–160.
Dahlen, F., 2005. Finite-frequency sensitivity kernels for boundary topography perturbations, *Geophys. J. Int.,* **162,** 525–540.
Dahlen, F.-A., Hung, S.-H. & Nolet, G., 2000. Fréchet kernels for finite frequency traveltimes-I. Theory, *Geophys. J. Int.,* **141,** 157–174.
Davies, C.J., Stegman, D.R. & Dumberry, M., 2014. The strength of gravitational core-mantle coupling, *Geophys. Res. Lett.,* **41,** 3786–3792.
Deschamps, F., Rogister, Y. & Tackley, P.J., 2018. Constraints on core-mantle boundary topography from models of thermal and thermochemical convection, *Geophys. J. Int.,* **212**(1), 164–188.
Doornbos, D.J. & Hilton, T., 1989. Models of core-mantle boundary and the travel times of internally reflected core phases, *J. geophys. Res.,* **94,** 15 741–15 751.
Doornbos, D.J. & Mondt, J.C., 1980. The interaction of elastic waves with a solid–liquid interface, with applications to the core-mantle boundary, *Pure appl. Geophys.,* **118,** 1293–1309.
Dziewoński, A.M. & Anderson, D.L., 1981. Preliminary reference Earth model, *Phys. Earth planet. Inter.,* **25,** 297–356.
Favier, N. & Chevrot, S., 2003. Sensitivity kernels for shear wave splitting in transverseisotropic media, *Geophys. J. Int.,* **153,** 213–228.
French, S.W. & Romanowicz, B.A., 2014. Whole-mantle radially anisotropic shear velocity structure from spectral-element waveform tomography, *Geophys. J. Int.,* **199**(3), 1303–1327.
Garcia, R. & Souriau, A., 2000. Amplitude of the core-mantle boundary topography estimated by stochastic analysis of core phases, *Phys. Earth planet. Inter.,* **117,** 345–359.
Garnero, E., McNamara, A. & Shim, S.-H., 2016. Continent-sized anomalous zones with low seismic velocity at the base of Earth's mantle, *Nat. Geosci.,* **9(7),** 481–489.
Garnero, E.J., 2000. Heterogeneity of the lowermost mantle, *Annu. Rev. Earth Planet. Sci.,* **28**(1), 509–537.
Gubbins, D. & Richards, M., 1986. Coupling of the core dynamo and mantle: Thermal or topographic?, *Geophys. Res. Lett.,* **13,** 1521–1524.
Gurnis, M., Wysession, M., Knittle, E. & Buffett, B., 1998. *The cOre-Mantle Boundary Region,* AGU.
Helffrich, G. & Wood, B., 2001. The Earth's mantle, *Nature,* **412,** 501.
Hirose, K., Sinmyo, R. & Hernlund, J., 2017. Perovskite in Earth's deep interior, *Science,* **358**(6364), 734–738.
Hung, S., Garnero, E., Chiao, L., Kuo, B.-Y. & Thorne, L., 2005. Finite frequency tomography of D″ shear velocity heterogeneity beneath the Caribbean, *J. geophys. Res.,* **110**(B7), 1–20.
Ishii, M. & Tromp, J., 1999. Normal-mode and free-air gravity constraints on lateral variations in velocity and density of Earth's mantle, *Science,* **285,** 1231–1236.
Jeanloz, R. & Williams, Q., 1998. The core-mantle boundary region, *Ultrahigh-Pressure Mineralogy: Physics and Chemistry of the Earth's Deep Interior, Rev. Mineral,* **37,** 241–259.
Koelemeijer, P., 2021. *Toward Consistent Seismological Models of the Core-mantle Boundary Landscape,* chap. 9, pp. 229–255, American Geophysical Union (AGU).
Koelemeijer, P.J., Deuss, A. & Trampert, J., 2012. Normal mode sensitivity to Earth's D″ layer and topography on the core-mantle boundary: what we can and cannot see, *Geophys. J. Int.,* **190**(1), 553–568.
Komatitsch, D. & Tromp, J., 1999. Introduction to the spectral element method for three-dimensional seismic wave propagation, *Geophys. J. Int.,* **139**(3), 806–822.
Komatitsch, D. & Tromp, J., 2002a. Spectral-element simulations of global seismic wave propagation-I. Validation, *Geophys. J. Int.,* **149**(2), 390–412.
Komatitsch, D. & Tromp, J., 2002b. Spectral-element simulations of global seismic wave propagation-II. 3-D models, oceans, rotation, and self-gravitation, *Geophys. J. Int.,* **150**(1), 303–318.
Komatitsch, D., Xie, Z., Bozdağ, E., Sales de Andrade, E., Peter, D., Liu, Q. & Tromp, J., 2016. Anelastic sensitivity kernels with parsimonious storage for adjoint tomography and full waveform inversion, *Geophys. J. Int.,* **206**(3), 1467–1478.
Koroni, M. & Trampert, J., 2016. The effect of topography of upper mantle discontinuities on *SS* precursors, *Geophys. J. Int.,* **204,** 667–681.
Koroni, M. & Trampert, J., 2021. Imaging global mantle discontinuities: a test using full-waveforms and adjoint kernels, *Geophys. J. Int.,* **226**(3), 1498–1516.
Koroni, M., Paulssen, H. & Trampert, J., 2019. Sensitivity kernels of PP precursor traveltimes and their limitations for imaging topography of discontinuities, *Geophys. Res. Lett.,* **46**(2), 698–707.
Krier, J., Thorne, M., Leng, K. & Nissen-Meyer, T., 2021. A compositional component to the Samoa Ultralow-Velocity Zone revealed through 2- and 3-D waveform modeling of SKS and SKKS differential travel-times and amplitudes, *J. geophys. Res.,* **126**(7), e2021JB021897 , doi:10.1029/2021JB021897.
Krischer, L., Megies, T., Barsch, R., Beyreuther, M., Lecocq, T., Caudron, C. & Wassermann, J., 2015. ObsPy: a bridge for seismology into the scientific python ecosystem, *Comput. Sci. Discovery,* **8,** 014003.
Lassak, T., McNamara, A., Garnero, E. & Zhong, S., 2010. Core–mantle boundary topography as a possible constraint on lower mantle chemistry and dynamics, *Earth planet. Sci. Lett.,* **289,** 232–241.
Lay, T., Williams, Q. & Garnero, E., 1998. The core–mantle boundary layer and deep Earth dynamics, *Science,* **392,** 461–468.
Lekic, V., Cottaar, S., Dziewonski, A. & Romanowicz, B., 2012. Cluster analysis of global lower mantle tomography: a new class of structure and implications for chemical heterogeneity, *Earth planet. Sci. Lett.,* **357-358,** 68–77.
Lessing, S., Thomas, C., Saki, M., Schmerr, N. & Vanacore, E., 2015. On the difficulties of detecting PP precursors, *Geophys. J. Int.,* **201,** 1666–1681.
Li, X.-D. & Romanowicz, B., 1996. Global mantle shear velocity model developed using nonlinear asymptotic coupling theory, *J. geophys. Res.,* **101**(B10), 22 245–22 272.
Li, X.-D., Giardini, D. & Woodhouse, J.H., 1991. Large-scale three-dimensional even-degree structure of the Earth from splitting of long-period normal modes, *J. geophys. Res.,* **96**(B1), 551–577.
Liu, Q. & Tromp, J., 2008. Finite-frequency sensitivity kernels for global seismic wave propagation based upon adjoint methods, *Geophys. J. Int.,* **174**(1), 265–286.
Luo, Y. & Schuster, G., 1991. Wave-equation traveltime inversion, *GeoRef* , doi:10.1190/1.1443081.
Mancinelli, N. & Shearer, P., 2016. Scattered energy from a rough core-mantle boundary modeled by a Monte Carlo seismic particle method: application to PKKP precursors, *Geophys. Res. Lett.,* **43**(15), 7963–7972.
Marquering, H., Dahlen, F. & Nolet, G., 1999. Three-dimensional sensitivity kernels for finite-frequency traveltimes: the banana-doughnut paradox, *Geophys. J. Int.,* **137**(3), 805–815.
Mattern, E., Matas, J., Ricard, Y. & Bass, J., 2005. Lower mantle composition and temperature from mineral physics and thermodynamic modelling, *Geophys. J. Int.,* **160**(3), 973–990.
McNamara, A., 2018. A review of large low shear velocity provinces and ultra low velocity zones, *Tectonophysics,* **760,** 199–220.
Morelli, A. & Dziewonski, A.M., 1987. Topography of the core-mantle boundary and lateral heterogeneity of the inner core, *Nature,* **325,** 678–683.
Muir, J. & Tkalčić, H., 2020. Probabilistic lowermost mantle P-wave tomography from hierarchical Hamiltonian Monte Carlo and model parametrization cross-validation, *Geophys. J. Int.,* **223**(3), 1630–1643.
Nissen-Meyer, T., van Driel, M., Stähler, S.C., Hosseini, K., Hempel, S., Auer, L., Colombi, A. & Fournier, A., 2014. AxiSEM: broadband 3-D seismic wavefields in axisymmetric media, *Solid Earth,* **5**(1), 425–445.
Obayashi, M. & Fukao, Y., 1997. P and PcP travel time tomography for the core-mantle boundary, *Geophys. J. R. astr. Soc.,* **102,** 17825–17841.
Rawlinson, N. & Kennett, B.L., 2004. Rapid estimation of relative and absolute delay times across a network by adaptive stacking, *Geophys. J. Int.,* **157**(1), 332–340.
Restivo, A. & Helffrich, G., 2006. Core-mantle boundary structure investigated using SKS and SKKS polarizartion anomalies, *Geophys. J. Int.,* **165**(1), 288–302.

Ritsema, J. & van Heijst, H.J., 2002. Constraints on the correlation of p- and s-wave velocity heterogeneity in the mantle from P, PP, PPP, and PKPab traveltimes, *Geophys. J. Int.,* **149,** 482–489.

Ritsema, J., Deuss, A., van Heijst, H. & Woodhouse, J., 2011. S40RTS:a degree-40 shear-velocity model for the mantle from new Rayleigh wave dispersion, teleseismic traveltime and normal-mode splitting function measurements, *Geophys. J. Int.,* **184(3),** 1223–1236.

Rodgers, A. & Wahr, J., 1993. Inference of core-mantle boundary topography from *ISC PcP* and *PKP* traveltimes, *Geophys. J. Int.,* **115,** 991–1011.

Rost, S. & Garnero, E.J., 2004. A study of the uppermost inner core from PKKP and PP differential traveltimes, *Geophys. J. Int.,* **156**(3), 565–574.

Schlaphorst, D., Thomas, C., Holme, R. & Abreu, R., 2016. Investigation of core-mantle boundary topography and lowermost mantle with P4KP waves, *Geophys. J. Int.,* **204**(2), 1060–1071.

Shen, Z., Ni, S., Wu, W. & Sun, D., 2016. Short period ScP phase amplitude calculations for core-mantle boundary with intermediate scale topography, *Phys. Earth planet. Inter.,* **253,** 64–73.

Sieminski, A., Paulssen, H., Trampert, J. & Tromp, J., 2008. Finite-frequency SKS splitting: Measurement and sensitivity kernels, *Bull. seism. Soc. Am.,* **98,** 1797–1810.

Soldati, G., Boschi, L. & Forte, A.M., 2012. Tomography of core-mantle boundary and lowermost mantle coupled by geodynamics, *Geophys. J. Int.,* **189**(2), 730–746.

Soldati, G., Koelemeijer, P., Boschi, L. & Deuss, A., 2013. Constraints on core-mantle boundary topography from normal mode splitting, *Geochem. Geophys. Geosyst.,* **14**(5), 1333–1342.

Souriau, A. & Poupinet, G., 1991. A study of the outermost liquid core using differential travel times of the SKS, SKKS and S3KS phases, *Phys. Earth planet. Inter.,* **68**(1), 183–199.

Stevenson, D., 1981. Models of the earth's core, *Science,* **214,** 611–619.

Sze, E.K. & van der Hilst, R.D., 2003. Core mantle boundary topography from short period PcP, PKP, and PKKP data, *Phys. Earth planet. Inter.,* **135**(1), 27–46.

Tanaka, S., 2002. Very low shear wave velocity at the base of the mantle under the South Pacific Superswell, *Earth Planet. Sci. Lett.,* **203**(3–4), 879–893.

Tanaka, S., 2010. Constraints on the core-mantle boundary topography from *P4KP-PcP* differential travel times, *J. geophys. Res.,* **115**(B4), 1–14.

Tanimoto, T., 1990. Long-wavelength S-wave velocity structure throughout the mantle, *Geophys. J. Int.,* **100**(3), 327–336.

Thorne, M.S. & Garnero, E.J., 2004. Inferences on ultralow-velocity zone structure from a global analysis of spdks waves, *J. geophys. Res.,* **109**(B8), doi:10.1029/2004JB003010.

Thorne, M.S., Garnero, E., Jahnke, G., Igel, H. & McNamara, A., 2013. Mega ultra low velocity zone and mantle flow, *Earth planet. Sci. Lett.,* **364,** 59–67.

Tromp, J., Tape, C. & Liu, Q., 2005. Seismic tomography, adjoint methods, time reversal and banana-doughnut kernels, *Geophys. J. Int.,* **160**(1), 195–216.

Whittaker, S., Thorne, M., Schmerr, N. & Miyagi, L., 2015. Seismic array constraints on the D″ discontinuity beneath Central America, *J. geophys. Res.,* **121**(1), 152–169.

Wu, W., Ni, S. & Shen, Z., 2014. Constraining the short scale core-mantle boundary topography beneath Kenai Peninsula (Alaska) with amplitudes of core-reflected PcP wave, *Phys. Earth planet. Inter.,* **236,** 60–68.

Yu, S. & Garnero, E., 2018. Ultralow velocity zone locations: a global assessment, *Geochem. Geophys. Geosyst.,* **19,** 396–414.